Integrated microprism and micro-electrode array for chronic in vivo two-photon imaging and electrophysiology across all cortical layers

Qianru Yang[1,2], Bingchen Wu[1,2], Elisa Castagnola[1], May Yoon Pwint[1,2], Alberto L. Vazquez[2,3,4], X. Tracy Cui[1,2,4]

[1] Department of Bioengineering, University of Pittsburgh, United States.

[2] Center for Neural Basis of Cognition, University of Pittsburgh and Carnegie Mellon University, United States.

[3] Department of Radiology, University of Pittsburgh, United States.

[4] McGowan Institute for Regenerative Medicine, University of Pittsburgh, United States.

Abstract

Implantable microelectrode arrays (MEAs) have been widely used for multisite neural recording and stimulation in basic neurophysiological research and brain-computer interface (BCI) applications. However, exactly how neural electrodes interact with brain cells remains poorly understood. Two-photon microscopy (TPM) is a valuable tool to observe cellular activities in vivo, but the imaging depth is usually limited to the superficial brain regions. In this work, we build a multi-functional device by integrating a microprism with a custom designed transparent MEA, allowing long-term sub cellular imaging, electrophysiological recording, and microstimulation in the same region across all cortical layers. The accessible depth is about six times deeper than the conventional method (~1000 µm vs. ~150 µm). By implanting this device in Thy1-GCaMP6s mice, we obtained stable TPM images of neuronal calcium activities across multiple cortical layers near the MEA, as well as single-unit recordings for 16 weeks. For the first time, we visualized the neuronal network activation pattern of all cortical layer in response to electrical stimulation with TPM, demonstrating the influence of stimulation location, amplitude, and frequency on neuronal activity. This novel MEA-on-microprism design provides a powerful multimodal method to investigate electrophysiology and cellular activities throughout all cortical layers in living animals.

Keywords

Microprism, brain-computer interface, electrophysiology, microstimulation, two-photon imaging

1. Introduction

1.1. Studies of the neuro-electronic interface using optical modalities

Intracortical neural electrodes have been a valuable tool in neuroscience research to record and manipulate brain activity [1-3]. These devices have also shown exciting potential as neural prosthetics to restore sensory and/or motor functions on patients with neurological deficits [4-6]. However, how neural electrodes interact with the brain tissue is not well understood. A comprehensive understanding of the relationship between electrophysiology and the brain activity is essential to improve the decoding efficiency and the engagement of relevant neuronal activity for neural prosthetics, as well as the accurate interpretation of electrode-based observations in neuroscience. Electrophysiological recordings are often used to readout activity evoked by intracortical stimulation [7, 8]. However, the inherent low throughput and low spatial resolution of recording electrodes fail to describe the activity of complex neuronal networks. Additionally, the artifact induced by electrical stimulation on electrophysiological recordings makes it difficult to identify the evoked responses by stimulation especially for electrodes close to the current injection site [9]. Optical imaging methodologies enable large scale neuronal activity measurements [10]. In vivo two-photon microscopy (TPM) combined with calcium imaging provides real-time monitoring of neuronal activities with sub-micron resolution [11-13], and has been used to reveal neuronal calcium dynamics of upper cortical layers (layer 1-3) in response to electrical stimulation in acute preparations [9, 14-16]. One limitation of previous in vivo two-photon imaging studies examining the tissue-electrode interface is that the electrodes must be inserted at ~30 degrees angle relative to the brain surface to accommodate the objective lens [17]. This angled insertion may cut the vertical layer-to-layer neuronal connections and is inconsistent with the most common application of intracortical brain-computer interface (BCI) where the electrodes are inserted vertically [18]. Additionally, prior acute in vivo TPM imaging studies of the brain-electrode interface have only focused on the top layers of the brain (layers 1-3) due to inevitable bleedings resulting from skull removal and electrode insertion [14, 15]. The laminar structure of the cortex is well-documented and the layer dependence of intracortical

electrodes has been reported in several studies using electrophysiology recordings or behavior tests [8, 19-21]. However, the cellular mechanisms of layer specificity pertaining to electrophysiological recording or stimulation remain poorly understood. Although recent advances have enabled volumetric TPM imaging of neuronal population calcium activity [22, 23], it has not been applied to brain tissue-electrode interface studies potentially because of the limitations and complications of the current setup. Moreover, the insertion of electrodes induces immediate inflammatory responses and interrupts normal neuronal calcium activities [24, 25]. These acute injury responses may confound our understanding of neural recording and microstimulation in chronic practice. Therefore, it is necessary to establish a chronic setup that allows imaging of multiple cortical layers past the acute surgical trauma phase.

Chronic two-photon imaging has been effectively used to examine the impact of electrode material for microstimulation on neuronal activity in the superficial cortex [26]. However, the imaging depth is more limited than acute preparations (up to ~150 µm deep). Many factors influence imaging depth including fibrous tissue formation, bone regrowth and the inflammatory response on the surface of the brain [27, 28]. Microprism implantation is a newly developed imaging technique that has great potential for investigating the brain tissue-electrode interface. By reflecting the light on the slant surface, microprisms (1x1x1 mm^3) provide a vertical view of the brain from the surface to ~1mm deep [29, 30]. In contrast to the conventional top-view which focuses on a horizontal plane relative to the objective lens, microprisms provide a novel perspective to observe cellular activities across multiple cortical layers using the same TPM imaging system. Previous studies have realized imaging of the vasculature, neuronal morphology, and calcium activities throughout all layers of the cortex with these microprisms [30-32]. Recently, our group evaluated the inflammatory responses to chronic microprism implantations in awake CX3CR1-GFP mice and showed that the inflammatory response subsides after about 8 weeks of implantation with a stable imaging window throughout our 32-week long study [33]. Here, we take advantage of this microprism preparation to investigate the chronic neural electrode-tissue interface at both superficial and deeper brain regions. Instead of inserting an electrode as a separate implant, we propose a transparent and flexible electrode array that is glued onto the vertical imaging surface of the microprism. This configuration does not introduce additional injury, mimics the implantation of larger arrays implanted vertically, and we use it to examine neuronal activity across multiple cortical layers.

1.2. Fabrication of microelectrode arrays with optical transparency

To combine electrode arrays with microprisms for chronic imaging, the transparency and flexibility of the device are essential. There has been an increasing trend and desire to develop transparent electrode arrays on flexible substrates that allow for concurrent imaging with electrophysiological recording [34-37], electrical stimulation [38], and optogenetic interrogation [39] of brain networks. Yet current developments have been limited to brain surface imaging.

Different transparent conductors have been used as electrode materials and integrated on flexible transparent parylene C and SU-8 insulator substrates. Transparent indium tin oxide (ITO)-μECoG arrays that consist of ITO microelectrodes with traces embedded in a transparent parylene C sheet have been shown to enable optogenetic manipulation and recording from the brain surface of rodents and non-human primates [39]. However, ITO is brittle and is susceptible to mechanical degradation when applied to situations where high flexibility is desired. An emerging material for transparent neural devices is graphene due to its high electron mobility, low thermal noise, flexibility, and optical transparency [40]. Transparent graphene microelectrode arrays have been shown to enable crosstalk-free integration with two-photon microscopy, optogenetic stimulation, and cortical recordings in the same in vivo experiments [40]. However, the high impedance of the graphene electrodes affects its sensitivity for neural recordings [41]. The electrodeposition of platinum nanoparticles (PtNPs) on transparent graphene electrodes can overcome this issue by drastically reducing the electrode impedance without significantly decreasing the optical transparency. Graphene/PtNP microelectrode arrays have been used for simultaneous in vivo calcium imaging while recording field potentials from the cortical surface [41]. In another study, fully transparent graphene electrodes enabled simultaneous electrical stimulation and calcium imaging of the underlying tissue in GCaMP6f mice [38]. Although promising results have been reported across several studies, all of them have recorded potential activity at the brain surface with large electrode sizes (2500-31400μm^2). The inherent low conductivity of ITO and graphene relative to typical metal materials limit the miniaturization of these devices for high resolution recording and stimulation.

On the other hand, several groups have been actively developing metal materials to create transparent MEAs. Qiang et al. used an innovative bilayer-nanomesh gold (Au) approach to create

a transparent MEA device [35]. In combination with template electroplating of poly(3,4-ethylenedioxythiophene)-poly(styrenesulfonate) (PEDOT:PSS) on gold (Au) nanomeshes, the final bilayer-nanomesh microelectrode surpassed the performance of previous graphene and ITO microelectrodes by more than one order of magnitude in both impedance and charge injection limit (CIL), enabling miniaturization of the MEA devices while slightly sacrificing optical transparency (67%). Liu et al. developed a flexible, self-insertable, and mostly transparent microelectrode array (Neuro-FITM) that enabled simultaneous wide-field optical imaging from the brain surface during electrophysiology recordings from the vertically inserted Neuro-FITM down to the hippocampus [42]. The transparent Parylene-C substrate and thin (2μm) Au wires minimize the shadow of the shank on the brain surface.

In this work, we sought to use a similar strategy to minimize the trace width in the region of the MEA that covers the imaging face of the microprism. Additionally, we designed a ring-shaped geometry for the metal recording/stimulation sites that allow light passage through the center to better image the tissue behind the electrode sites while maintaining the same geometric area as commonly used 30μm-diameter round electrode sites. Nano-Pt was electrochemically deposited onto the electrode sites to improve their electrochemical performance as a stimulation material. We also developed protocols to assemble the functional MEA on the microprism device and finally tested our microprism/ MEA assembly chronically in Thy1-GCaMP6 mice. Here we present the results of in vivo two-photon calcium imaging, electrophysiological recording, and microstimulation from our integrated MEA-on-microprism device for up to 16 weeks post implantation. To the best of our knowledge, this is the first exploration that combines microprism and MEA for studying neuroelectronic interface chronically and the first in vivo TPM study illustrating the neuronal calcium activity across multiple cortical layers in response to microstimulation.

2. Results

We developed a platform that combined a flexible microelectrode array with a microprism to enable chronic TPM imaging of neuronal activity around the functional neuroelectronic interface in a vertical plane spanning from the brain surface to cortical layer 5/6.

1.1. Manufacturing the MEA-on-microprism device

The microelectrode arrays were fabricated using standard micro-fabrication photolithography techniques as described in detail in the Materials and Methods section and in Figure 1. The insulating SU-8 layers have a total thickness of approximately 18 µm, allowing them to be ultra-flexible and conformable to the surface of the microprism device. The 4x4 MEA configuration covers an area of 600 x 600 μm^2 with a vertical and horizontal inter-electrode spacing of 200 µm (center-to-center) (figure 1f). Within the 1 x 1 mm^2 face ("tip") region, the width of the metal traces is reduced to 2 µm and the contacting sites adopt a ring-shaped design to reduce light blockage while maintaining the desired electrophysiological performance of typical microelectrode sites. The ring site has an external diameter of 50 µm and an internal diameter of 40 µm, the same geometric area (706 μm^2) as a standard 30 µm-diameter round electrode.

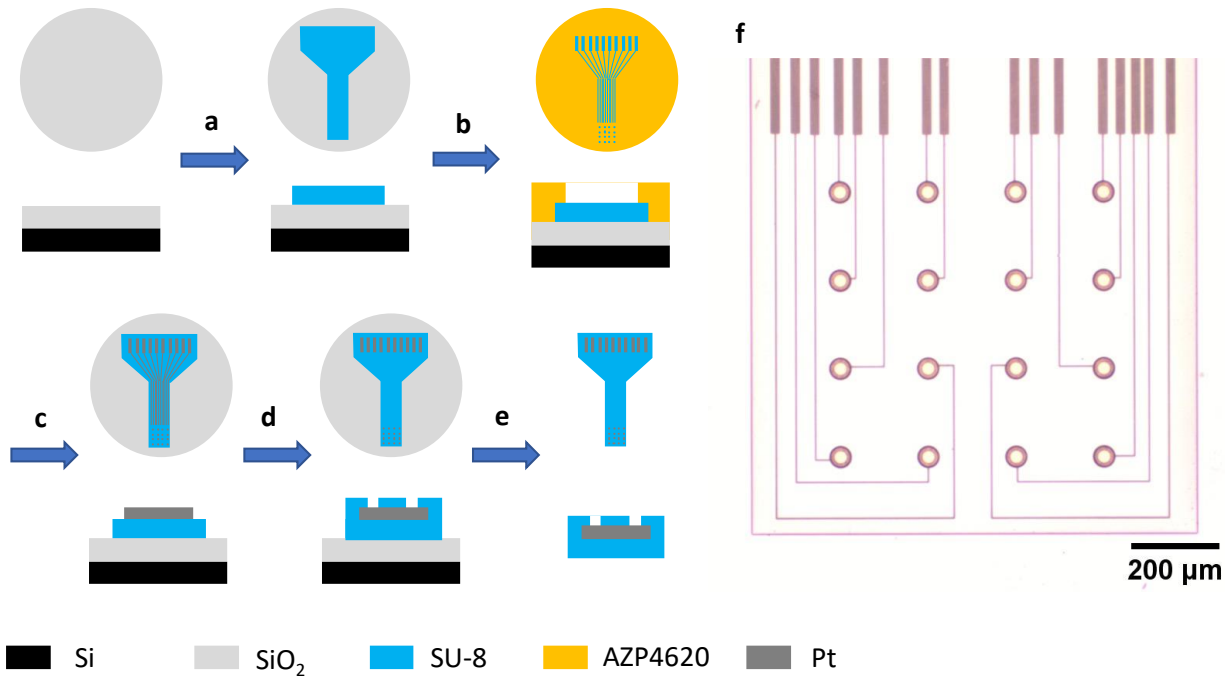

Figure 1. Fabrication of the flexible and transparent MEA.

(a)~(e) Schematic of photolithography procedures. The top view and the side view of each step are shown in stack (dimensions not to scale). (a) SU-8 is spin coated, exposed, and then developed as the bottom insulation on a silicon (Si) wafer with 1µm of silicon dioxide (SiO_2) on the top. (b) AZ4620 positive photo resist is spin coated, exposed, and developed as the mask for the metal layer. (c) Platinum (Pt) is evaporated on the wafer and lifted-off in acetone to form the conductive metal part. (d) Another layer of SU-8 is spin coated, exposed, and developed as the

top insulation. (e) The wafer is placed in buffered oxide etchant to release the MEA device. (f) Optical microscopy image of the face ("tip") region of the MEA showing the 4x4 ring-shaped array and the thin connecting traces.

We then electrochemically deposited a nano-Pt coating on the ring-shaped microelectrodes with high spatial precision as seen in the SEM images (figure 2a). The magnified SEM of the nano-Pt coating shows a cauliflower-like nanostructured morphology, which is strikingly different from the relative flat surface of a bare Pt electrode. These images clearly show that the nano-Pt coating drastically increases the effective electrochemical area of the electrode. In accordance with the SEM, we observed a significant increase in the charge storage capacity (CSC) of the electrode from 1.06±0.15 mC cm^{-2} to 6.05±0.17 mC cm^{-2}, as calculated from the time integral of the last cyclic voltammogram (CV) cycle before and after the nano-Pt coating (Figure 2b). We also observed that the nano-Pt coating decreased the impedance of the electrode in the low frequency range (Figure 2c). Specifically, the impedance at 1kHz dropped from 75.32±23.70 kΩ to 41.34±2.96 kΩ. After nano-Pt deposition, the CIL of the electrode is estimated to be 2.27mC cm^{-2}, as we can deliver 80 µA cathodic current for 200 µs before the E_{mc} reaches -0.6V verses Ag/AgCl (Figure 2d).

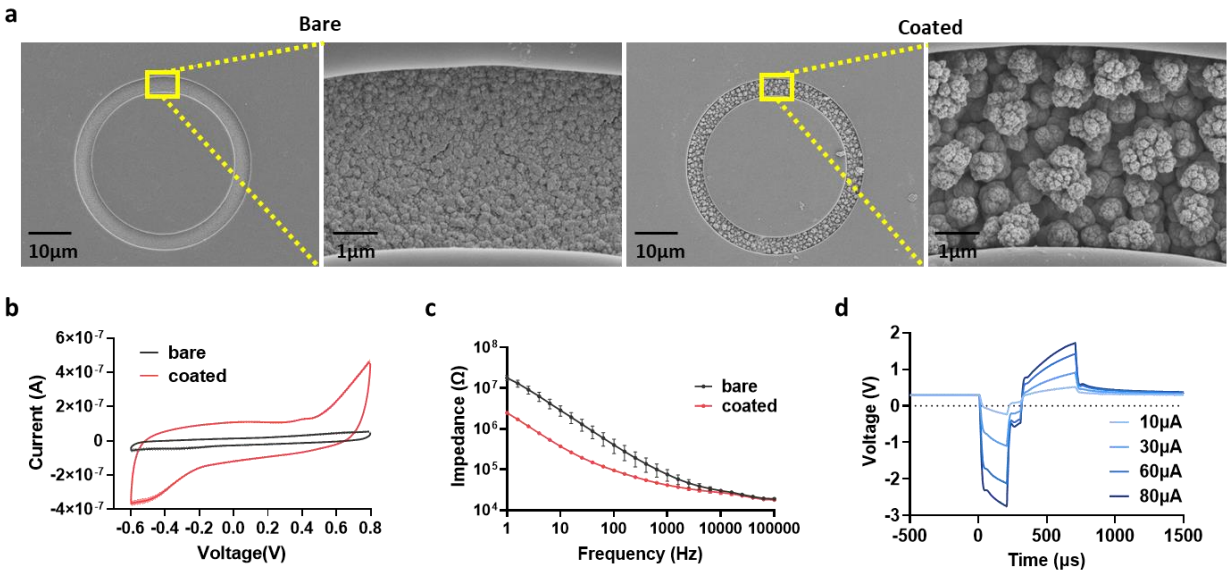

Figure 2. Representative SEM images and in vitro electrochemical properties of MEA before and after nano-Pt deposition.

(a) Representative SEM images of bare and nano-Pt coated electrode sites. Magnified views on the right side in each condition show the nanostructured surface morphologies. (b) CV of a representative MEA before and after nano-Pt coating. N=16 electrode sites. Data are presented as mean ± SD. (c) Electrochemical impedance spectroscopy (EIS) of a MEA before and after nano Pt coating. N=16 electrode sites. Data are presented as mean ± SD. (d) Voltage transients in response to bi-phasic, asymmetric ($I_c = 2 * I_a$) current pulses. The cathodic current amplitudes were ramped up from 10 µA to 80 µA.

The procedure to assemble a functional microprism/MEA device is illustrated in figure 3. We designed and purchased the 16-channel PCB that connects the Omnetics connector with 16 metal pads and two metal rings for ground/reference electrode. The MEA was bonded to the PCB with a silver heat-seal cable. We tested the CV and EIS of the MEA to ensure proper connections. To improve the electrochemical properties of electrodes, we electrochemically deposited nano-Pt onto the Pt electrode sites. In addition, the microprism was attached to three pieces of coverglass by a transparent optical glue. Then we carefully adhered the tip of MEA to the microprism and the coverglasses. Finally, we soldered a silver wire to the ground and reference pads on the PCB and applied a thin layer of silicone onto the traces and wires to strengthen the insulation and the mechanical durability of the device. We ran electrochemical characterizations of the fully assembled device and sterilized it with ETO sterilization before the implantation surgery.

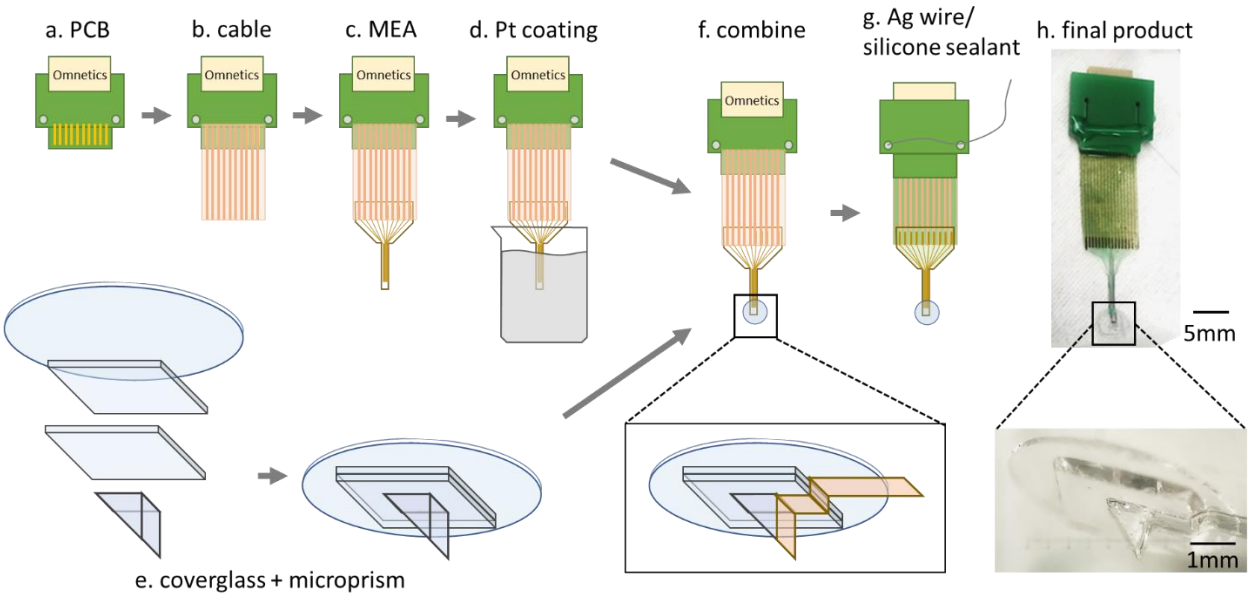

Figure 3. Assembly procedure of the functional MEA-on-microprism device.

(a) Customized PCB with standard 16-channel Omnetics connector. (b) Connect the heat-seal cable to the metal traces on PCB. (c) Bond our previously fabricated MEA to the heat-seal cable. (d) Electrochemically deposit nano-Pt onto MEA by applying a constant voltage. (e) Glue microprism and three pieces of coverglasses together using a UV-cured transparent glue. (f) Adhere the tip of MEA to the microprism's imaging face using the transparent glue. (g) Solder a silver wire to the PCB as the ground/reference. Spread a thin layer of silicone sealant onto the backside of the cable, the trace region on MEA, and cover all the exposed bare metal part. (h) Photo of a finished assembly. Inset reveals the magnified view of MEA tip on the microprism. Scale bar=5mm for the top photo, and 1mm for the inset.

1.2. Long-term in vivo TPM, single-unit recordings, and microstimulation achieved using the MEA-on-microprism device

The surgical procedure is similar to implanting just the microprism as described in previous publications [29, 30, 33]. We created a 4mm x 4mm square cranial window over the right hemisphere of the animal. After removing dura matter, we made a 1mm long and 1mm deep cut and inserted the microprism/MEA vertically into the incision. The difference from just a microprism implantation is that we used another stereotaxic arm to hold the PCB tab in addition

to the one that controls the microprism. Close attention needs to be paid to the position of the two stereotaxic arms when moving either of them to avoid shear force that may easily tear the device. The MEA was grounded to a stainless-steel bone screw on the contralateral skull. The connector and PCB tab were fixed to the skull with dental cement embedding (figure 4a).

Successful surgery can maintain a clear and stable cranial window for over 16 weeks (figure 4b). Through the implanted microprism, we were able to monitor neuronal activities from the brain surface down to layer 5/6, confirmed by the void in expression of layer 4 neurons in Thy1-GCaMP6s animals (figure 4c). Aligned with previous work [33], the imaging distance is around 500 µm from the microprism vertical face after several weeks of recovery. It is evident that the ring shape design allows light to pass through the ring, so that the tissue behind the electrodes can be imaged. Due to the propagation of light around and through the rings, the shadow of the thin metal traces is almost invisible beyond 50 µm from the microprism while the electrode site shadows become invisible beyond 200 µm from the microprism (figure 4c).

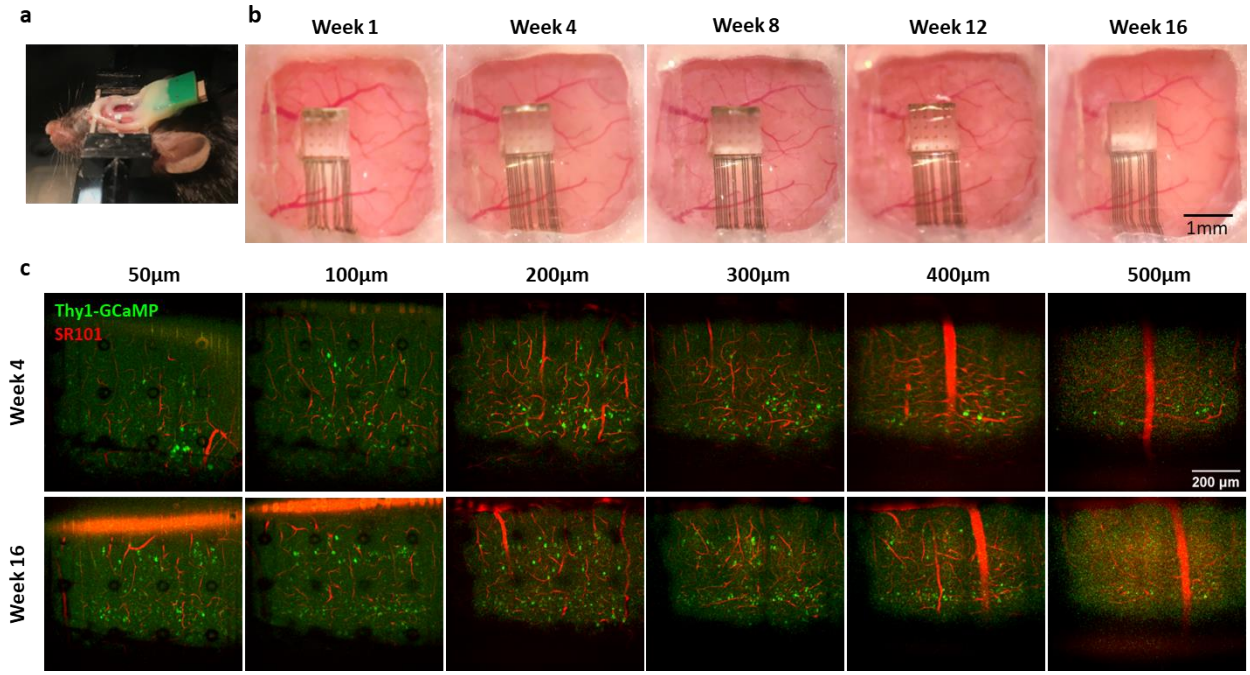

Figure 4. Two-photon images through the MEA-on-microprism device at different chronic time points from one live animal.

(a) Bird's eye view of the cranial window and the device on a head fixed mouse. (b) Images of the cranial window under the surgical microscope for over 16 weeks. (b) Imaging of spontaneous

neural activities (green) and blood vessels (red) through microprism. Left to right: focused on different distances from the microprism.

We characterized the electrochemical properties of the MEAs implanted on three animals in vivo using a two-electrode setup, where a stainless-steel bone screw on the contralateral brain hemisphere served as the counter electrode. Note that for in vitro electrochemical measurements we used a three-electrodes setup, thus the results are not directly comparable. We analyzed 22 electrode sites from three animals that maintained a reasonable 1kHz impedance (<1 MΩ) at most of the times. The CSC of individual electrode sites fluctuate over time as shown in figure 5a. The average CSC also possesses ups and downs over time—it increased in the first week then dropped back and reached the lowest value at week 2, followed by a slight increasing trend afterwards (figure 5a). The CSC at week12 and week 16 were significantly higher than day 0 (immediately after the implantation surgery) (figure 5a). The mean impedance at 1kHz of the MEAs increased in the first 2 weeks, then declined from week 2 to week 8, and increased back from week 8 to week 16 (figure 5b). The impedance at week 2, week 6 and week 8 was significantly different from day 0 (figure 5b). The shape of the CV curve and the impedance spectrum change from a representative electrode site are plotted over time in figure 5c and 5d. In the first 2 weeks, the CV graph of this representative site shrunk by about half. While at weeks 4 and 8, the CV almost returned to its original shape. Later at weeks 12 and 16 post-surgery, the CV curves broadened evidently (figure 5c). The impedance of this electrode site increased a little from day 0 to week 2 (figure 5d), which may indicate the formation of glial scars. After week 4, the impedance decreased in all frequencies and remained low compared to day 0 (figure 5d). In accordance, the voltage transients induced by the same 5uA pulse curves, the E_{mc} decreased from around -1 V (week 2) to -0.6 V (week 4~ week 16) (figure 5e). The widened CV curve after week 12 and the impedance drop across frequencies indicate that the effective electrochemical surface area of the electrode has increased [43]. This phenomenon could be explained by insulation cracking or liquid penetrating under the insulation layer [44, 45]. Despite this, the changes of CSC and impedance at 1kHz for most sites stayed within the same magnitude throughout 16 weeks, showing the long-term stability of our custom-fabricated MEA.

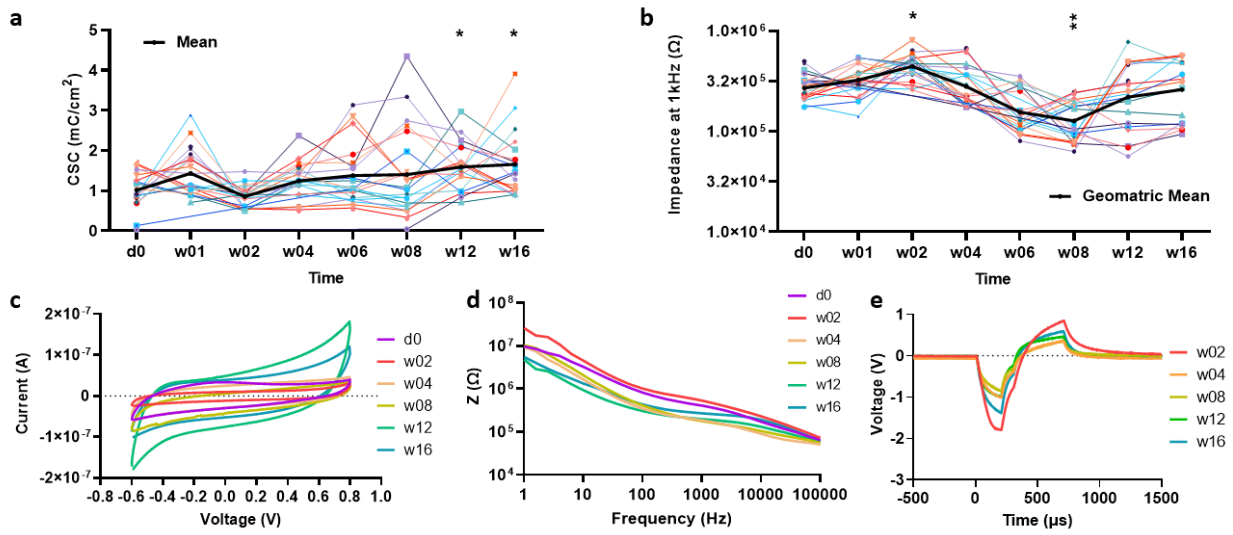

Figure 5. In vivo electrochemical properties of MEA

(a) Charge storage capacity of the MEA over time (n=22 sites from 3 animals). Individual sites are plotted in assorted colors, and the mean value is presented in thick black line. (b) Impedance at 1kHz over time (n=22 sites from 3 animals). Individual sites are plotted in assorted colors, and the mean value is presented in thick black line. In (a) & (b), we ran a one-way ANOVA followed by Dunn's multiple comparison to test for differences against time point d0. * $p<0.05$, ** $p<0.01$. (c) Representative CV curve of one electrode site over time. Different colors indicate different time points. (d) Representative impedance spectrum of one electrode site over time. Different colors indicate different time points as in (c). (e) Representative voltage transients in response to the same current pulse (bi-phasic, asymmetric, 5µA cathodic leading) over time. Different colors indicate different time points.

The implanted MEA was able to record single-unit activities on resting awake animals for over 16 weeks (figure 6). Spike waveforms are sorted using the automatic k-means feature in Offline Sorter software. Noise clusters were manually excluded.

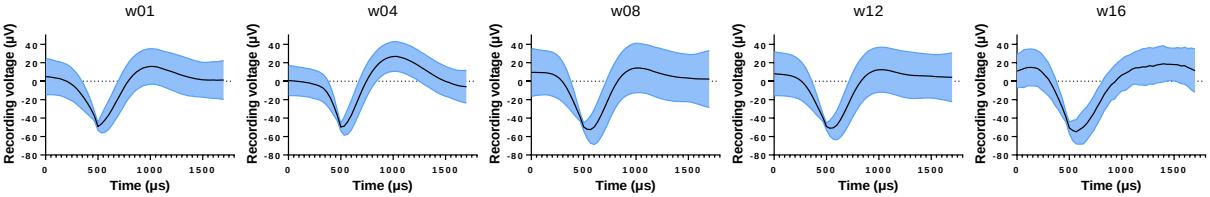

Figure 6. Example spikes from electrophysiological recordings

Representative spike waveforms over time. Waveforms are extracted from 2-min spontaneous recordings from head-fixed, awake mice using Offline Sorter software. Data are presented as mean ± SD.

Next, we examined the TPM imaging of neuronal activity evoked by visual stimulation. A blue LED light was placed about 5 cm away from the contralateral eye of the mouse. After a 30-sec delay, the LED light flickers for 1 sec at 10Hz every 15 sec. By averaging 10 trials, we identified the neurons that were repetitively activated by the light stimuli (figure 7a). The relative fluorescent intensity change (ΔF/F) of three representative neurons during the whole session are shown in figure 7b. The background fluorescent intensity (F) is the mean value of the first 30 sec before light stimulation. These curves corroborate that these neurons are responding to the light stimulations. After aligning the curves to the time stamp of light stimuli from the 10 trials, we learn the average response of each neuron (figure 7c). Neuron #1 and neuron #2 peak at the light-on period, while neuron #3 show the largest response after light-off (figure 7c). These are typical responses of neurons that are sensitive to a light spot being turned on or off in the visual system [46-48]. These results indicate that the visual input circuits are preserved near the microprism/MEA face, showing the potential for studying all kinds of sensory evoked neuronal responses with this device. Simultaneous TPM imaging and recording from the MEA has been explored, but the huge photo-electric artifact deteriorates electrophysiology signals so much that we can hardly extract any meaningful information from the recording during laser scan. To achieve TPM and recording at the same time, future works could consider replacing the Pt with low photo-electric effect materials.

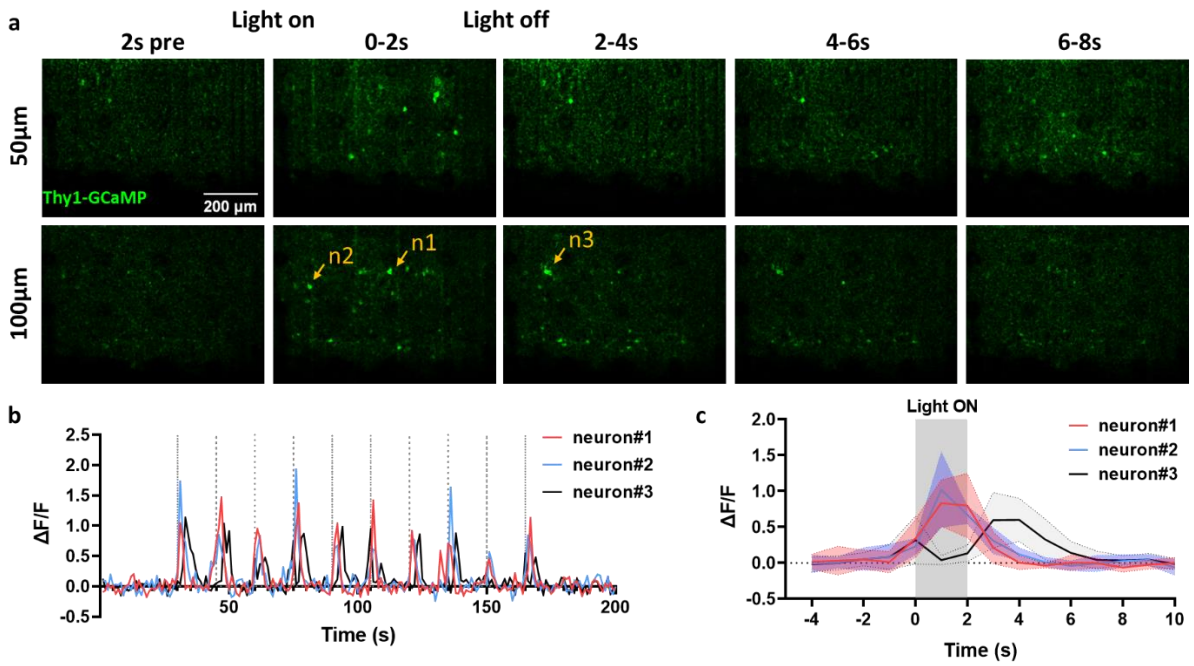

Figure 7. TPM imaging of visual stimulation (light pulses) evoked neuronal calcium responses. (a) GCaMP fluorescence changes before/during/after light stimulation. Averaged from 10 consecutive trials. n1~n3 mark the three neurons analyzed in (b) and (c). (b) GCaMP fluorescence change of three representative neurons during the whole 200s imaging session. Dotted lines indicate the on-set time of each light stimulation period (1 sec). (c) Averaged fluorescence change of the three neurons relative to the light stimuli. The line with shadow represents mean ± SD.

We also conducted TPM imaging of neuronal responses to electrical stimulation delivered through the MEA on the microprism. Electrical stimulation consisted of charge-balanced square wave pulses with 200 µs cathodic phase, 100 µs interval and 400 µs anodic phase (figure 8a), mimicking the parameters used in human studies [4]. The reported amplitudes here all refer to the cathodic current amplitudes. We first asked how the current amplitude of stimulation influences neuronal activation. We stimulated every available site with impedance of < 1MOhm at 1kHz three times with 25% duty cycle (1s ON, 3s OFF) at 50Hz and monitored the neuronal calcium activity 50µm away from the MEA surface using TPM in awake mice. The images were averaged from three stimulation periods. Near the activation threshold current (5µA), a couple of sparsely distributed neurons were activated (figure 8b). As we increased the

current amplitude to 10µA, more neurons near the stimulated electrode became activated (figure 8b). When the current amplitude reached 15µA, we observed a lot of neuropil activation around the stimulated site and that the neural response appeared to saturate at >15µA (figure 8b). Similar neuronal calcium responses to changing amplitudes were observed on all working electrode sites over different days. The sparse and distributed neuronal activation at 5µA is consistent with a previous TPM study [9], while here we have a vertical observation plane across all cortical layers instead of focusing on a single horizonal plane in layer 2/3. We chose 10µA for the rest of stimulation experiments as it was just sufficient to reliably generate an obvious neural calcium response for most sites. Note that the Thy1-GCaMP6 expression is lower in layer 4 than other cortical layers [49], we use the fluorescent dark band at around 400µm deep as a reference marker for cortical layer 4 (figure 8b, c).

Next, we investigated how the stimulation location affects the cortical neural network activity in response to electrical stimuli. Current pulse trains (1s, 10µA) were delivered at 50Hz from the MEA while imaging neuronal calcium responses under TPM (Supplementary Video 1). We observed that electrical stimulations from the same column of the MEA activated a similar group of neurons but with different strengths (figure 8c, Ch1~Ch4). Additionally, electrical stimulations at another column recruited a different cohort of neurons (figure 8c, Ch5~Ch6), indicating a columnar neural activation field. To qualitatively compare the strength and the distribution of the neural calcium activation, we further plotted the profile of fluorescent intensity change along X and Y axis (figure 8d and e). The layer 4 (Ch2) electrode was found eliciting the strongest GCaMP response, layer 5 (Ch3) electrode the second, layer 2/3 (Ch1) and layer 6 (Ch4) electrodes lower. These results indicate that electrical stimulation may be most efficient at activating neuronal populations in general if delivered at layer 4, followed by layer 5, and less efficient at layer 2/3 and layer 6 in this stimulation paradigm. After we normalized the fluorescent intensity to the peak intensity value for each site in figure 8e, we noticed higher relative peaks at around 500µm deep for Ch2 and Ch6 compared to their layer2/3 neighbor electrodes Ch1 and Ch5 (figure 8f). These observations indicate that apart from the overall stimulation power, layer 4 electrode sites recruit relatively more deep layer (L5) neurons compared to layer 2/3 electrode sites. The impedance spectrums of these electrode sites were similar but not completely overlapping (Supplementary Figure 1), confirming that these

electrode sites were not shorted and that the difference in neural activation was unlikely to result from variability of individual electrode sites.

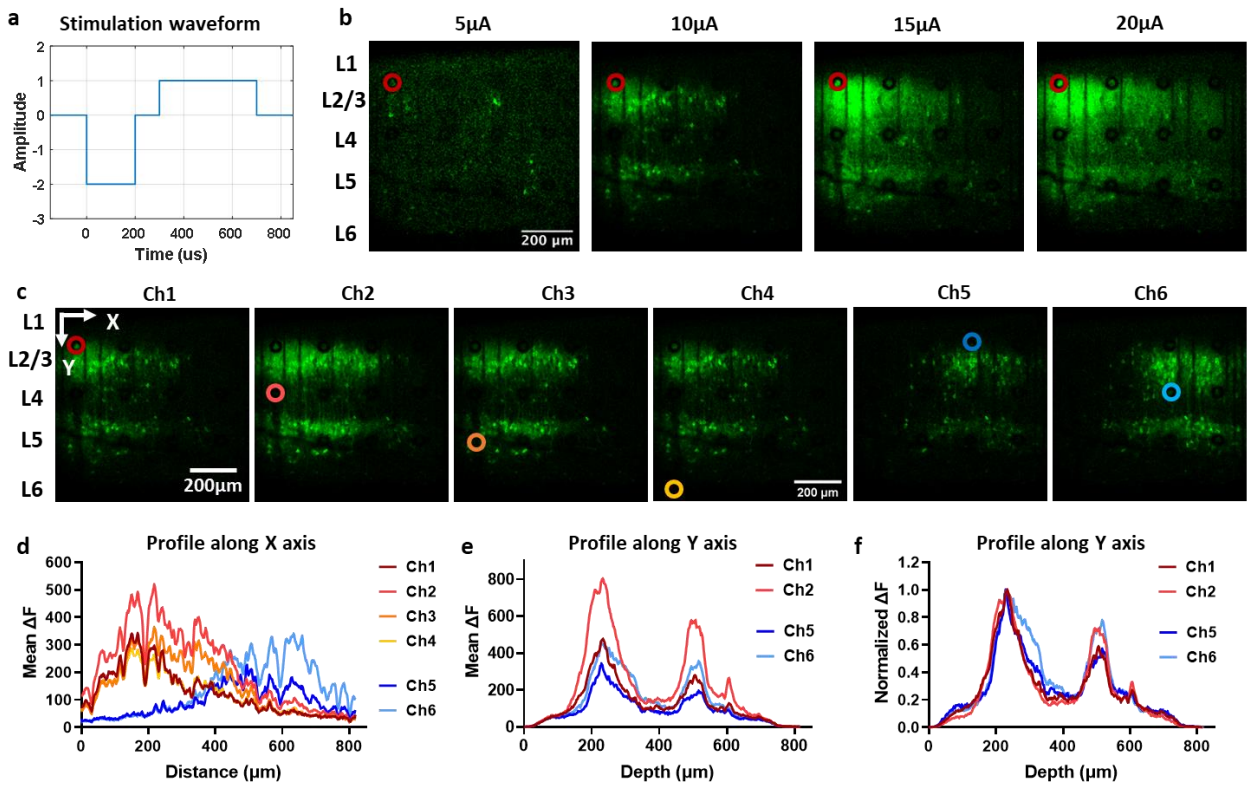

Figure 8. TPM imaging of neuronal responses to electrical stimulation reveals amplitude and location dependence.

(a) The electrical stimulation waveform used. (b) Representative TPM images of neuronal calcium activity change in response to electrical stimulation at increasing current amplitudes. The images are averaged over three repetitions of stimulation for each amplitude. The red circle indicates the location of the stimulated channel. (c) Representative TPM images of neuronal calcium activity change in response to electrical stimulation at different locations. The images are averaged over three repetitions for each electrode site. The circles in gradient colors indicate the location of the stimulated channel. (d) The fluorescent intensity profile of images in (c) projected along the x-axis. (e) The fluorescent intensity profile of images in (d) projected along the y-axis. (f) Normalized fluorescent intensity profile along y-axis.

In addition to the current amplitude and electrode location, frequency is also a crucial factor that can modulate the neural response to electrical stimulation. Changing the stimulation frequency has been shown to alter the type of tactile sensation and the perception intensity in the somatosensory cortex [4, 50, 51]. There is also behavioral evidence indicating that frequency modulation of intracortical stimuli is layer-specific [20]. However, the mechanism of frequency modulation on the neural network level remains to be elucidated. With this in mind, we stimulated all the available channels of the MEA at various frequencies, ranging from 5Hz to 150Hz, while keeping the same amplitude (10 µA). Again, using in vivo TPM imaging through our device, we found that increasing the frequency of stimulation affects the neuronal activation pattern in a complex manner. Taking a layer 4 electrode site as an example: at 5Hz, the neural activation was sparse and distributed; as we increased the frequency to 50Hz, the neuronal response was much stronger, but still distributed; when we further increased the frequency, the intensity decreased, and the field of neuronal activation shrunk (figure 9a and b). Interestingly, although the overall neuronal activation decreased from 50Hz to 150Hz, more neurons at around 400 µm deep were activated at higher frequencies (figure 9a and c). Moreover, the frequency modulation curve may be also depth-dependent. Within the same column of electrodes on the MEA, the middle layer electrode sites (Ch2 and Ch3) induced the strongest overall neuronal response at ~50Hz, while electrodes at the superficial layer (Ch1) or at the deep layer (Ch4) induced larger neuronal responses at 20Hz compared to other frequencies tested (figure 9d).

These stimulation experiments concerning depth dependence have been replicated in the same animal over different days. Although three of four animals survived at least 16 weeks of implantation (75% survival rate), two of them were excluded from the stimulation analysis due to poor imaging clarity or a liquid gap between the MEA and the brain tissue. Future studies may seek strategies to improve the biocompatibility of MEA materials and further investigate the depth dependence of intracortical microstimulation with greater number of animals, finer step size in depth, and fluorescent labeling of other types of cells.

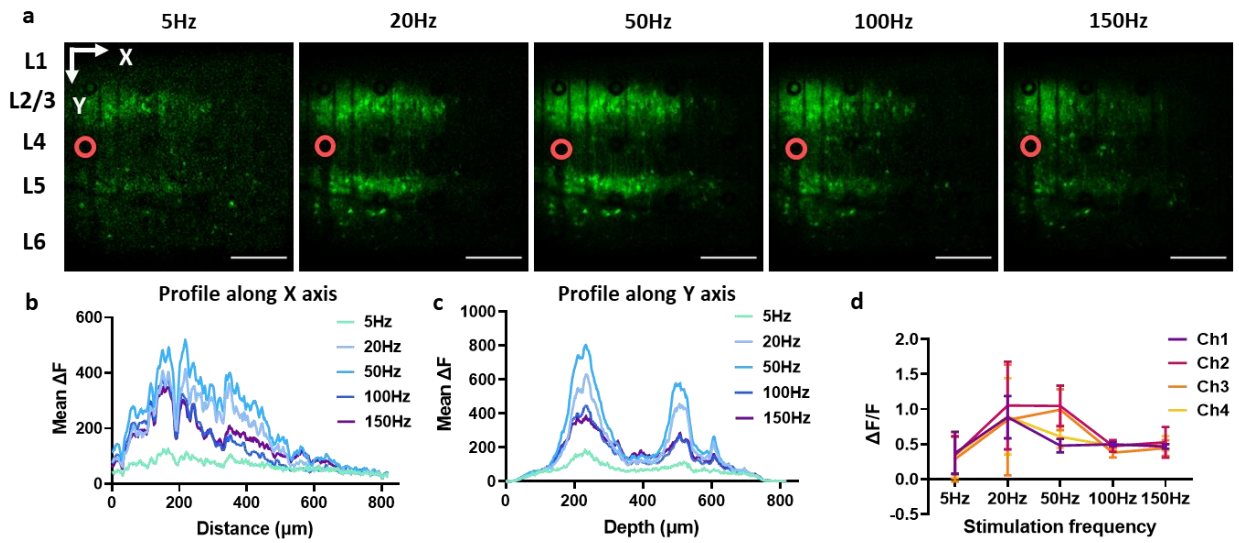

Figure 9. TPM imaging of neuronal responses to electrical stimulation reveals frequency dependence and depth dependence.

(a) Representative TPM images of neuronal calcium activity in response to electrical stimulation from an L4 site at increasing frequencies. The stimulations are bi-phasic, asymmetric square wave pulses at 10µA (cathodic) for 1 sec. The images are averaged from three repetitions of stimulation. The red circle indicates the location of the stimulated channel. This imaging plane is focused at 50µm from the MEA. Scale bar=200µm. (b) The fluorescent intensity profile of images in (a) projected to the x-axis. (c) The fluorescent intensity profile of images in (a) projected to the y-axis. (d) Frequency dependence curves of electrodes at different depths (Ch1~4). N=6 stimulations on two separate days.

3. Conclusions

In this work we combine for the first time a 1-mm microprism with an MEA, providing a powerful tool for both optical imaging and electrophysiological modulation across multiple cortical layers over long time scales. The custom-fabricated MEA achieves high flexibility and transparency by photolithographically patterning platinum on a flexible and transparent SU-8 substrate, plus ring-shaped electrode sites and thin traces that minimize the shadow of metal in the region of imaging. This novel MEA-on-microprism design remarkably expands the vertical depth of chronic two-photon imaging of electrode arrays from ~150 µm to ~1000 µm, allowing

for electrophysiology and in vivo imaging across multiple cortical layers in the same region. With this setup, we were able to perform chronic TPM imaging and electrical recording/stimulation in Thy1-GCaMP6s mice for over 16 weeks. High-resolution TPM images of neuronal calcium activities near the MEA have been captured at the resting state and upon sensory stimuli of the animal. We observed stable in vivo electrochemical properties of the MEA and demonstrated its capability of single unit recording throughout 16 weeks of implantation. Furthermore, using this device, we demonstrated how electrode location, stimulation amplitude, and stimulation frequency influence the neuronal calcium responses to intracortical microstimulation. To the best of our knowledge, this is the first in vivo TPM imaging work that directly visualizes the cortical multi-layer neuronal network activation pattern as a result of microstimulation. This technology will not only advance our understanding of in vivo electrophysiological recordings and microstimulation at the cellular and cortical network level but also provide a powerful tool for neuroscience research and BCI technology development with multiple modalities.

4. Methods

4.1. Fabrication of MEA

Microelectrode arrays (MEA) fabrication: Si wafer with 1µm thick SiO2 layer (University Wafer Inc) was first cleaned by sonicating in acetone, isopropanol, and DI water sequentially for 5 mins each step. The wafer was then dried on hot plate at 150°C for 3 mins and cleaned by O_2 plasma using reactive ion etcher (RIE, Trion Phantom III LT) for 120s at 200 mTorr pressure and 150Watts power. The cleaned wafer was spin-coated with SU-8 2015 (MicroChemicals) at 5000rpm for 1min and soft baked at 65°C for 3 mins and 95°C for 5 mins. Then the wafer was exposed using a maskless aligner (MLA, MLA100 Heidelberg Instruments) with a dose of 400 mJ/cm2. After exposure, the SU-8 first layer was post baked at 65°C for 3 mins and 95°C for 5 mins, developed using SU-8 developer (MicroChemicals) for 1min and cleaned by isopropanol and DI water and hard baked at 200°C, 180°C, and 150°C for 5mins each and allowed to cool down below 95°C. The wafer was then treated with O_2 plasma with RIE for 75s at pressure of 200 mTorr and 150W power. The cleaned wafer was then spin-coated with AZ P4620 photoresist (MicroChemicals) at 5300rpm for 1min and baked at 105°C for 5mins. After

baking the wafer is exposed using MLA with a dose of 700mJ/cm2, then developed using AZ400k 1:4 developer (MicroChemicals), cleaned by water rinsed, and dried by N2 gas flow. A mild 60s RIE O2 plasma cleaning at pressure 600 mTorr and 60W power was perform before metal deposition. 10nm Ti adhesion layer and 100nm Pt layer were evaporated on the wafer using Electron Beam Evaporator (Plassys MEB550S). Then the metal was lifted-off in acetone overnight. The next day, the wafer was cleaned by O2 plasma for 60s at 600 mTorr and 60W, then spin-coated with SU-8 2015 at 5000rpm for 1min and soft baked at 65°C for 2 mins and 95°C for 5 mins. The wafer is exposed using MLA with a dose of 400mJ/cm2, post backed, and developed with SU-8 developer. The wafer was then cleaned by isopropanol and water, and hard baked at 200°C, 180°C, and 150°C for 5mins each and allowed to cool down below 95°C. The MEAs were lifted-off from the wafer using buffered oxide etchant (1:7) in acid hood for 8 hours.

4.2. Electrodeposition of Pt

Nano-platinum was electrochemically formed starting from a solution containing 25mM $H_2(PtCl_6)$ in 1mM HCl, by applying a constant voltage at -0.3V for 200s. Electrochemical depositions were carried out using a potentiostat/galvanostat (Autolab, Metrohm, USA), connected to a three-electrode electrochemical cell with a platinum counter electrode and an Ag/AgCl reference electrode.

4.3. Assembly of microprism and MEA

Similar to previous work, microprism was purchased (#MPCH-1.0, Tower Optical Corporation) and adhered to three layers of coverglasses (two 3x3mm square, one 5mm round, #1 thickness, 0.15 ± 0.02 mm, Warner Instruments LLC) using a transparent glue (NOA 71, Norland Optical).

The printed circuit board (PCB) was manufactured following a customized design. The MEA was connected to the PCB using a silver heat-seal connector (P/N HST-9805-210, Elform). Specifically, the connector cable was trimmed to fit the width of PCB and MEA with a length of 1~2cm. The cable was then aligned and bonded to the PCB and MEA using a hair straightener heated to 380°F for ~30s with pressure. Two pieces of PDMS (~1mm thick) were used to pad between the heating pad and the PCB/MEA on both sides. After electrochemically depositing nanoplatinum onto the sites, we applied a drop of NOA 71 glue to the back side of MEA tip and

carefully adhered the MEA to the microprism imaging face and the coverglasses, with an angled tip tweezer holding the MEA bent at ~90 degrees at the corner. Excess glue that ran to the front side of MEA was gently removed with a fine tip tweezer. The ground and reference site on the PCB were connected to a silver wire, which will be wired around the bone screw on the animal later. Finally, all the exposed traces and fragile parts were covered with a thin layer of silicone to provide additional insulation and mechanical support. Fully assembled devices were characterized with electrochemical methods described below and sterilized with the ethylene oxide sterilization process before surgery.

4.4. Electrochemical characterizations

Electrochemical impedance spectroscopy (EIS) and cyclic voltammetry (CV) measurements were used to investigate the electrode/solution interface in vitro, prior to implantation, and in vivo.

During the EIS measurements, a sine wave (10 mV RMS amplitude) was superimposed onto the open circuit potential while varying the frequency from 1 to 10^5 Hz. During the CV tests, the working electrode potential was swept between 0.8V and −0.6 V with a scan rate of 1V/s. Both EIS and CV measurements were carried out using a potentiostat/galvanostat (Autolab, Metrohm, USA).

In vitro, EIS and CV were performed in 1x phosphate buffered saline (PBS, composition: 11.9 mM Na_2HPO_4 and KH_2PO_4, 137 mM NaCl, 2.7 mM KCl, pH 7.4) using a three-electrode electrochemical cell configuration with a platinum counter electrode and an Ag/AgCl reference electrode.

In the brain, EIS and CV were measured using a two-electrode electrochemical cell configuration, where a stainless-steel bone screw, anchored on the contralateral skull, served as the counter and reference electrode.

4.5. Animals and surgery

Transgenic mice expressing the neuronal activity reporter GCaMP6s in cortical pyramidal neurons (male, n=3, strain Tg (Thy1-GCaMP6s) GP4.3Dkim) were used in this study and obtained from the Jackson Laboratories (Bar Harbor, ME USA). During surgery, mice were

anesthetized using ketamine (75mg/kg)/xylazine(10mg/kg) and maintained with updates of ketamine (22.5mg/kg) alone as needed. Animal fur on top of the head was trimmed off and the skin surface was then sterilized with 70% isopropyl alcohol and betadine. The animal head was fixed onto a stereotaxic frame (Narishige International USA) and the temperature kept at 37 °C with an electric heating pad. After skin resection and skull drying with Vetbond (3M, St. Paul, MN), a rectangular stainless-steel frame (#CF-10, Narishige International USA) was adhered onto the skull with dental cement (A-M Systems, Sequim, WA). We waited until the dental cement completely solidified before transferring the animal to a frame-holding stereotax (Narishige International USA). A stainless-steel bone screw (0.86mm shaft diameter, Fine Science Tools, Inc.) was secured on the left parietal bone of the skull as reference and ground for the electrode. Using a high-speed dental drill, we created a 4x4 mm craniotomy above the somatosensory and visual cortex over the right hemisphere. The dura matter within the cranial window was removed with fine tip tweezer and a bent 30-gauge needle. A lance-shaped 0.1 mm thick razor blade (#72000, Electron Microscopy Sciences) was attached to a stereotaxic arm and inserted vertically then moved laterally to create a 1x1 mm incision. We applied saline and Gelfoam on the surface of the brain and waited for bleedings to stop. The PCB of the device was anchored to a stereotaxic arm angled at about 30 degrees and was approaching the cranial window from the back of the animal. Another stereotaxic arm was oriented vertically to hold the cover glass of the microprism/MEA with a vacuum line. The microprism/MEA was inserted vertically into the incision, with the imaging surface of microprism facing posterior (visual cortex) of the animal. The microprism/MEA device was lowered until the round coverglass touched the skull so that the square coverglasses were contacting brain surface with a little pressure to prevent dura and meningeal regrowth. Tiny drops of silicone sealant (Kwik-sil, World Precision Instruments) were applied around the coverglass and on the uncovered brain surface if any to seal the cranial window. The vacuum was released after dental cement secured the implant in place. The ground/reference wire was connected to the bone screw. Excessive cable was folded to the back of the PCB and covered with dental cement. After surgery, the animal was treated with 5 mg/kg ketofen (100 mg/ ml, Zoetis Inc., Kalamazoo, MI) and 10mg/kg Baytril solution (Henry Schein Inc.) for three days. All experimental protocols were approved by the University of Pittsburgh, Division of Laboratory Animal Resources and Institutional Animal Care and Use Committee (ARO ID: IS00018691) in accordance with the standards for humane

animal care as set by the Animal Welfare Act and the National Institutes of Health Guide for the Care and Use of Laboratory Animals.

4.6. In vivo two-photon imaging and image processing

The animal was head-fixed, free-running on a custom treadmill during two-photon imaging. The two-photon imaging system has been described in our previous publications [25, 33]. It consists of an ultra-fast laser (Insight DS+; Spectra-Physics, Menlo Park, CA), a scan head (Bruker, Madison, WI), non-descanned photomultiplier tubes (Hamamatsu Photonics KK, Hamamatsu, Shizuoka, Japan), and a 16X 0.8 NA water immersion objective lens (Nikon Instruments, Melville, NY). The excitation laser was set at wavelength of 920 nm. Sulforhodamine 101 (SR101) (~0.05 cc; 1 mg/ml) was injected before imaging for visualization of blood vessels. For imaging neuronal calcium activities, time-series images were collected at 512 x 512 x 1 pixels and at ~1 frames per second (fps).

The time-series images were processed and analyzed using ImageJ and customized IJ1 macro scripts. The images were first denoised with a median filter and the “Despeckle” function. A background image was acquired by averaging the whole image stack or the images before any stimulation. Then we subtract the background image from every image in the time series. The resulting fluorescence change images were maximum intensity projected to a single image to capture all active neurons during the period of interest. The vasculature in figure 4 is the average image of the red (SR101) channel, which is superimposed to the above neural activity image in green (Thy1-GCaMP) channel.

For quantification of neuronal calcium intensity change in Figure 7, we manually circled the neurons from the raw image stack, and exported the intensity change over time. The fluorescent intensity change ratio ($\Delta F/F$) is then calculated, where F is the mean value of fluorescence intensity in the first 30s before light stimulation, and ΔF is the difference between F and the fluorescent at each time stamp. In figure 8 and figure 9, the fluorescent intensity profile along x and y axis is measured with the “Plot profile” function in ImageJ. The image was rotated 90 degrees to change the direction of profile projection.

4.7. Electrophysiological recording

Electrophysiological recording was performed on awake animals. Data was collected by Ripple Grapevine (Nano2+stim Ripple LLC, Salt Lake City, Utah) and Trellis software at 30kHz sample rate. Spike waveforms were sorted in Plexon offline sorter (version 3) using the spike trains data. We first applied K-means automatic sorting algorithm to the raw data in all the channels. Then we checked the waveforms of each unit and discarded the incorrect units.

4.8. Electrical stimulation

Current-controlled stimulations were delivered using Autolab (Metrohm, USA). 1-sec long pulse trains contain biphasic, charge-balanced asymmetric square waves with various amplitudes and frequencies. Each pulse has a 200 µs cathodic phase, a 100 µs interval and a 400 µs anodic phase. The anodic current amplitude is set at half of the cathodic current. During one imaging session, each electrode site is stimulated three times in a row; each time there is a 1-sec stimulation period and a 3-sec off period.

5. Acknowledgement

The authors thank Dr. Hui Fang and Dr. Qiang Yi for advice and materials on the heat-seal connector. This work is supported by NIH R01NS089688 and BRAIN R01NS110564.

6. Table of Contents

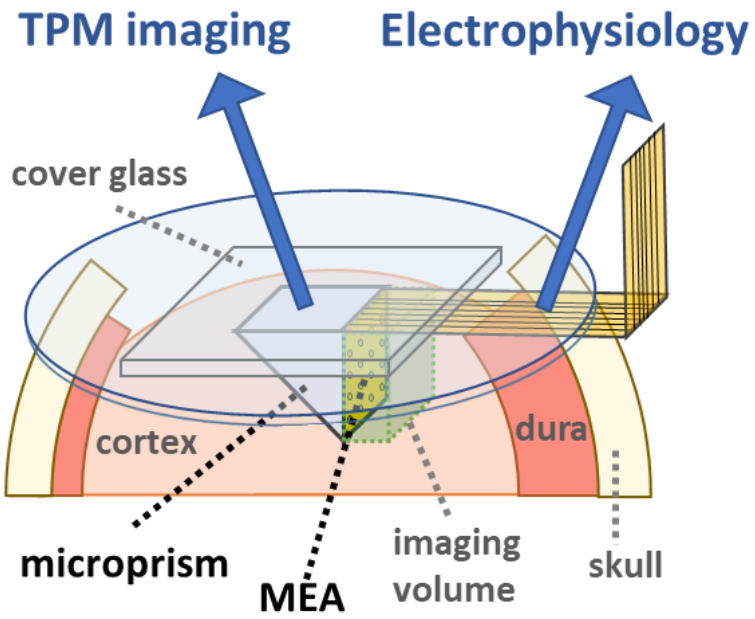

This novel MEA-on-microprism device combines a microprism with a flexible and mostly transparent microelectrode array. It enables long-term, sub-micron resolution two-photon imaging of the brain tissue-electrode interface across multiple cortical layers in living animals. This multi-functional device can help us understand the cellular activity in the brain during electrical recordings/stimulations.

References

[1] H. Asanuma, S. Stoney Jr, C. Abzug, Relationship between afferent input and motor outflow in cat motorsensory cortex, Journal of Neurophysiology 31(5) (1968) 670-681.
[2] W.G. Penfield, Ferrier lecture-some observations on the cerebral cortex of man, Proceedings of the Royal Society of London. Series B-Biological Sciences 134(876) (1947) 329-347.
[3] E. Bizzi, Discharge of frontal eye field neurons during saccadic and following eye movements in unanesthetized monkeys, Experimental Brain Research 6(1) (1968) 69-80.
[4] S.N. Flesher, J.L. Collinger, S.T. Foldes, J.M. Weiss, J.E. Downey, E.C. Tyler-Kabara, S.J. Bensmaia, A.B. Schwartz, M.L. Boninger, R.A. Gaunt, Intracortical microstimulation of human somatosensory cortex, Science translational medicine 8(361) (2016) 361ra141-361ra141.
[5] G.A. Tabot, J.F. Dammann, J.A. Berg, F.V. Tenore, J.L. Boback, R.J. Vogelstein, S.J. Bensmaia, Restoring the sense of touch with a prosthetic hand through a brain interface, Proceedings of the National Academy of Sciences 110(45) (2013) 18279-18284.
[6] W.H. Dobelle, Artificial vision for the blind by connecting a television camera to the visual cortex, ASAIO journal 46(1) (2000) 3-9.
[7] S. Stoney Jr, W. Thompson, H. Asanuma, Excitation of pyramidal tract cells by intracortical microstimulation: effective extent of stimulating current, Journal of neurophysiology 31(5) (1968) 659-669.
[8] M.B. Voigt, P. Hubka, A. Kral, Intracortical microstimulation differentially activates cortical layers based on stimulation depth, Brain stimulation 10(3) (2017) 684-694.
[9] M.H. Histed, V. Bonin, R.C. Reid, Direct activation of sparse, distributed populations of cortical neurons by electrical microstimulation, Neuron 63(4) (2009) 508-522.
[10] A.A. Brock, R.M. Friedman, R.H. Fan, A.W. Roe, Optical imaging of cortical networks via intracortical microstimulation, Journal of neurophysiology 110(11) (2013) 2670-2678.
[11] W. Denk, J.H. Strickler, W.W. Webb, Two-photon laser scanning fluorescence microscopy, Science 248(4951) (1990) 73-76.
[12] K. Svoboda, W. Denk, D. Kleinfeld, D.W. Tank, In vivo dendritic calcium dynamics in neocortical pyramidal neurons, Nature 385(6612) (1997) 161-165.
[13] C. Stosiek, O. Garaschuk, K. Holthoff, A. Konnerth, In vivo two-photon calcium imaging of neuronal networks, Proceedings of the National Academy of Sciences 100(12) (2003) 7319-7324.
[14] K.C. Stieger, J.R. Eles, K.A. Ludwig, T.D. Kozai, In vivo microstimulation with cathodic and anodic asymmetric waveforms modulates spatiotemporal calcium dynamics in cortical neuropil and pyramidal neurons of male mice, Journal of neuroscience research 98(10) (2020) 2072-2095.
[15] J.R. Eles, T.D. Kozai, In vivo imaging of calcium and glutamate responses to intracortical microstimulation reveals distinct temporal responses of the neuropil and somatic compartments in layer II/III neurons, Biomaterials 234 (2020) 119767.
[16] N.J. Michelson, J.R. Eles, A.L. Vazquez, K.A. Ludwig, T.D. Kozai, Calcium activation of cortical neurons by continuous electrical stimulation: Frequency dependence, temporal fidelity, and activation density, Journal of neuroscience research 97(5) (2019) 620-638.
[17] (!!! INVALID CITATION !!! [20, 21, 28, 29]).
[18] (!!! INVALID CITATION !!! [30-32]).
[19] T. Allison-Walker, M.A. Hagan, N.S. Price, Y.T. Wong, Microstimulation-evoked neural responses in visual cortex are depth dependent, Brain Stimulation 14(4) (2021) 741-750.
[20] M.E. Urdaneta, N.G. Kunigk, F. Delgado, S.I. Fried, K.J. Otto, Layer-specific parameters of intracortical microstimulation of the somatosensory cortex, Journal of Neural Engineering 18(5) (2021) 055007.

[21] M.E. Urdaneta, N.G. Kunigk, S. Currlin, F. Delgado, S.I. Fried, K.J. Otto, The Long-Term Stability of Intracortical Microstimulation and the Foreign Body Response Are Layer Dependent, Frontiers in Neuroscience (2022) 849.
[22] A. Song, A.S. Charles, S.A. Koay, J.L. Gauthier, S.Y. Thiberge, J.W. Pillow, D.W. Tank, Volumetric two-photon imaging of neurons using stereoscopy (vTwINS), Nature methods 14(4) (2017) 420-426.
[23] M.B. Bouchard, V. Voleti, C.S. Mendes, C. Lacefield, W.B. Grueber, R.S. Mann, R.M. Bruno, E.M. Hillman, Swept confocally-aligned planar excitation (SCAPE) microscopy for high-speed volumetric imaging of behaving organisms, Nature photonics 9(2) (2015) 113-119.
[24] J.R. Eles, A.L. Vazquez, T.D. Kozai, X.T. Cui, In vivo imaging of neuronal calcium during electrode implantation: spatial and temporal mapping of damage and recovery, Biomaterials 174 (2018) 79-94.
[25] T.D.Y. Kozai, A.L. Vazquez, C.L. Weaver, S.-G. Kim, X.T. Cui, In vivo two-photon microscopy reveals immediate microglial reaction to implantation of microelectrode through extension of processes, Journal of neural engineering 9(6) (2012) 066001.
[26] X.S. Zheng, Q. Yang, A. Vazquez, X.T. Cui, Imaging the efficiency of PEDOT/CNT and iridium oxide electrode coatings for microstimulation.
[27] T.D. Kozai, J.R. Eles, A.L. Vazquez, X.T. Cui, Two-photon imaging of chronically implanted neural electrodes: Sealing methods and new insights, Journal of neuroscience methods 258 (2016) 46-55.
[28] J. Eles, A. Vazquez, T. Kozai, X. Cui, Meningeal inflammatory response and fibrous tissue remodeling around intracortical implants: an in vivo two-photon imaging study, Biomaterials 195 (2019) 111-123.
[29] T.H. Chia, M.J. Levene, Microprisms for in vivo multilayer cortical imaging, Journal of neurophysiology 102(2) (2009) 1310-1314.
[30] M.L. Andermann, N.B. Gilfoy, G.J. Goldey, R.N. Sachdev, M. Wölfel, D.A. McCormick, R.C. Reid, M.J. Levene, Chronic cellular imaging of entire cortical columns in awake mice using microprisms, Neuron 80(4) (2013) 900-913.
[31] R.J. Low, Y. Gu, D.W. Tank, Cellular resolution optical access to brain regions in fissures: imaging medial prefrontal cortex and grid cells in entorhinal cortex, Proceedings of the National Academy of Sciences 111(52) (2014) 18739-18744.
[32] L. Beckmann, X. Zhang, N.A. Nadkarni, Z. Cai, A. Batra, D.P. Sullivan, W.A. Muller, C. Sun, R. Kuranov, H.F. Zhang, Longitudinal deep-brain imaging in mouse using visible-light optical coherence tomography through chronic microprism cranial window, Biomedical optics express 10(10) (2019) 5235-5250.
[33] Q. Yang, A.L. Vazquez, X.T. Cui, Long-term in vivo two-photon imaging of the neuroinflammatory response to intracortical implants and micro-vessel disruptions in awake mice, Biomaterials 276 (2021) 121060.
[34] C.F. Guo, T. Sun, Q. Liu, Z. Suo, Z. Ren, Highly stretchable and transparent nanomesh electrodes made by grain boundary lithography, Nature communications 5(1) (2014) 1-8.
[35] Y. Qiang, P. Artoni, K.J. Seo, S. Culaclii, V. Hogan, X. Zhao, Y. Zhong, X. Han, P.-M. Wang, Y.-K. Lo, Transparent arrays of bilayer-nanomesh microelectrodes for simultaneous electrophysiology and two-photon imaging in the brain, Science advances 4(9) (2018) eaat0626.
[36] W. Lee, D. Kim, N. Matsuhisa, M. Nagase, M. Sekino, G.G. Malliaras, T. Yokota, T. Someya, Transparent, conformable, active multielectrode array using organic electrochemical transistors, Proceedings of the National Academy of Sciences 114(40) (2017) 10554-10559.
[37] D. Kuzum, H. Takano, E. Shim, J.C. Reed, H. Juul, A.G. Richardson, J. De Vries, H. Bink, M.A. Dichter, T.H. Lucas, Transparent and flexible low noise graphene electrodes for simultaneous electrophysiology and neuroimaging, Nature communications 5(1) (2014) 1-10.
[38] D.-W. Park, J.P. Ness, S.K. Brodnick, C. Esquibel, J. Novello, F. Atry, D.-H. Baek, H. Kim, J. Bong, K.I. Swanson, Electrical neural stimulation and simultaneous in vivo monitoring with transparent graphene electrode arrays implanted in GCaMP6f mice, ACS nano 12(1) (2018) 148-157.

[39] P. Ledochowitsch, A. Yazdan-Shahmorad, K. Bouchard, C. Diaz-Botia, T. Hanson, J.-W. He, B. Seybold, E. Olivero, E. Phillips, T. Blanche, Strategies for optical control and simultaneous electrical readout of extended cortical circuits, Journal of neuroscience methods 256 (2015) 220-231.
[40] M. Thunemann, Y. Lu, X. Liu, K. Kılıç, M. Desjardins, M. Vandenberghe, S. Sadegh, P.A. Saisan, Q. Cheng, K.L. Weldy, Deep 2-photon imaging and artifact-free optogenetics through transparent graphene microelectrode arrays, Nature communications 9(1) (2018) 1-12.
[41] Y. Lu, X. Liu, R. Hattori, C. Ren, X. Zhang, T. Komiyama, D. Kuzum, Ultralow impedance graphene microelectrodes with high optical transparency for simultaneous deep two-photon imaging in transgenic mice, Advanced functional materials 28(31) (2018) 1800002.
[42] X. Liu, C. Ren, Y. Lu, Y. Liu, J.-H. Kim, S. Leutgeb, T. Komiyama, D. Kuzum, Multimodal neural recordings with Neuro-FITM uncover diverse patterns of cortical–hippocampal interactions, Nature Neuroscience 24(6) (2021) 886-896.
[43] S.R. Kane, S.F. Cogan, J. Ehrlich, T.D. Plante, D.B. McCreery, P.R. Troyk, Electrical performance of penetrating microelectrodes chronically implanted in cat cortex, IEEE Transactions on Biomedical Engineering 60(8) (2013) 2153-2160.
[44] B.J. Black, A. Kanneganti, A. Joshi-Imre, R. Rihani, B. Chakraborty, J. Abbott, J.J. Pancrazio, S.F. Cogan, Chronic recording and electrochemical performance of Utah microelectrode arrays implanted in rat motor cortex, Journal of neurophysiology 120(4) (2018) 2083-2090.
[45] S.F. Cogan, Neural stimulation and recording electrodes, Annu. Rev. Biomed. Eng. 10 (2008) 275-309.
[46] L.A. Palmer, T.L. Davis, Receptive-field structure in cat striate cortex, Journal of neurophysiology 46(2) (1981) 260-276.
[47] E.D. Adrian, R. Matthews, The action of light on the eye: Part I. The discharge of impulses in the optic nerve and its relation to the electric changes in the retina, The Journal of Physiology 63(4) (1927) 378.
[48] W. Bair, J.R. Cavanaugh, M.A. Smith, J.A. Movshon, The timing of response onset and offset in macaque visual neurons, Journal of Neuroscience 22(8) (2002) 3189-3205.
[49] H. Dana, T.-W. Chen, A. Hu, B.C. Shields, C. Guo, L.L. Looger, D.S. Kim, K. Svoboda, Thy1-GCaMP6 transgenic mice for neuronal population imaging in vivo, PloS one 9(9) (2014) e108697.
[50] C.L. Hughes, S.N. Flesher, J.M. Weiss, M. Boninger, J.L. Collinger, R.A. Gaunt, Perception of microstimulation frequency in human somatosensory cortex, ELife 10 (2021) e65128.
[51] T. Callier, N.W. Brantly, A. Caravelli, S.J. Bensmaia, The frequency of cortical microstimulation shapes artificial touch, Proceedings of the National Academy of Sciences 117(2) (2020) 1191-1200.

Supplementary materials

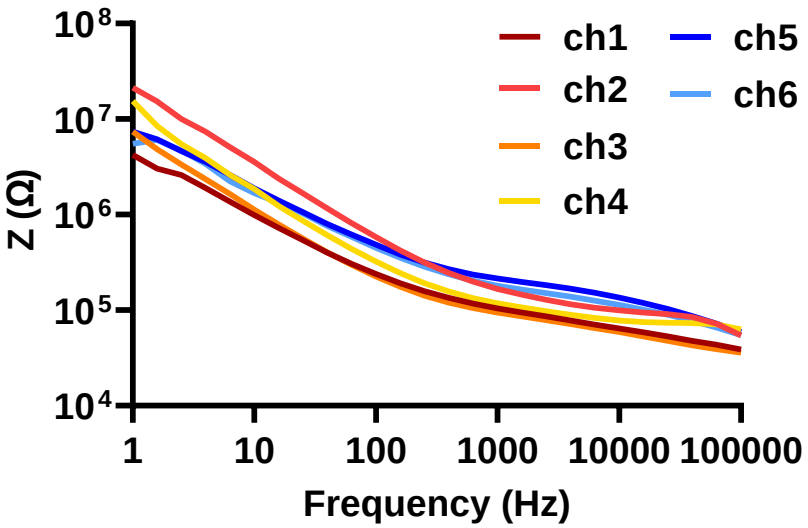

Supplementary figure 1. Impedance spectrum of the electrode sites presented in figure 8 on the day of stimulation.